

# E-Calib: A Fast, Robust and Accurate Calibration Toolbox for Event Cameras

Mohammed Salah, Abdulla Ayyad, Muhammad Humais, Daniel Gehrig, Abdelqader Abusafieh, Lakmal Seneviratne, Davide Scaramuzza, and Yahya Zweiri

**Abstract**—Event cameras triggered a paradigm shift in the computer vision community delineated by their asynchronous nature, low latency, and high dynamic range. Calibration of event cameras is always essential to account for the sensor intrinsic parameters and for 3D perception. However, conventional image-based calibration techniques are not applicable due to the asynchronous, binary output of the sensor. The current standard for calibrating event cameras relies on either blinking patterns or event-based image reconstruction algorithms. These approaches are difficult to deploy in factory settings and are affected by noise and artifacts degrading the calibration performance. To bridge these limitations, we present E-Calib, a novel, fast, robust, and accurate calibration toolbox for event cameras utilizing the asymmetric circle grid, for its robustness to out-of-focus scenes. The proposed method is tested in a variety of rigorous experiments for different event camera models, on circle grids with different geometric properties, and under challenging illumination conditions. The results show that our approach outperforms the state-of-the-art in detection success rate, reprojection error, and estimation accuracy of extrinsic parameters.

CODE AND MULTIMEDIA MATERIAL

Video:

<https://youtu.be/4giQn6rt-48>

Code and Dataset:

[https://github.com/mohammedsalah98/E\\_Calib](https://github.com/mohammedsalah98/E_Calib)

## I. INTRODUCTION

OVER the past decades, imaging sensors have evolved at a rapid pace providing solutions for various intelligent perception algorithms. The event camera is a bio-inspired sensor whose pixels are *smart* and *independent* of each other: when a pixel detects a change of intensity (usually triggered by motion), that pixel triggers an *event*, which records the

coordinates of the pixel spiking, the time at which the event occurred, and the sign of the intensity change. The output of an event camera is therefore not frames at constant time intervals but rather an asynchronous stream of events in space and time. Due its asynchronous and differential nature, an event camera has three key advantages for robot manufacturing: sub-millisecond latency, microsecond resolution, and very high dynamic range [1]–[3]. These features grant the sensor robustness against motion blur and poorly lighted environments, marking a new paradigm for vision sensors. With such unprecedented capabilities in hand, event-based vision unveiled its impact in space robotics [4]–[6], robotic manufacturing [7], fast object detection and tracking [8]–[11], autonomous navigation [12]–[14], and indoor positioning systems [15].

In all of the aforementioned applications, calibration of the event camera is a necessary prerequisite to account for sensor intrinsics and for pose estimation. Due to the asynchronous, spatially sparse, binary output of events, conventional calibration methods are not applicable for calibrating event cameras. Calibration of the earliest event camera models was attained using blinking calibration patterns [16], but require extensive instrumentation. A more practical method evolved relying on event-based image reconstruction algorithms [17], where calibration was attained using conventional image-based calibration methods. Nevertheless, the reconstructed images suffer from artifacts and sensor noise degrading the calibration accuracy.

More sophisticated event camera models, also called Dynamic Active-Pixel Vision Sensor (DAVIS) [18], are accompanied by frame-based imaging capabilities, where the active-pixel sensor (APS) frames are utilized for calibration using conventional calibration techniques. As event-based vision is gradually gaining maturity, recent models of event cameras are rather manufactured as stand-alone sensors. Thus, Huang et al. [19] proposed a multi-segment optimization-based approach to obtain the event camera intrinsics from the asynchronous events using the asymmetric circle grid for its robustness against defocused scenes. However, the approach utilizes the event stream as control points for the calibration optimization. Hence, sub-pixel localization accuracy of the calibration feature points is not attained degrading the calibration accuracy. This ultimately instigates a surging demand for a robust, event-driven calibration tool to obtain the intrinsic parameters of event cameras.

The drawbacks of the previously mentioned methods show that an accurate calibration tool is needed for event cameras and is attained with the following: 1) Robustness to sensor

This work was supported by the Advanced Research and Innovation Center (ARIC), which is jointly funded by STRATA Manufacturing PJSC (a Mubadala company), Khalifa University of Science and Technology in part by Khalifa University Center for Autonomous Robotic Systems under Award RC1-2018-KUCARS, and Sandooq Al Watan under Grant SWARD-S22-015.

M. Salah, A. Ayyad, and Y. Zweiri are with the Advanced Research and Innovation Center (ARIC), Khalifa University, Abu Dhabi, UAE. Y. Zweiri is also with the Department of Aerospace Engineering and is the director of the Advanced Research and Innovation Center.

M. Humais and L. Seneviratne are with the Center for Autonomous Robotic Systems, Khalifa University, Khalifa University, Abu Dhabi, UAE, and L. Seneviratne is the director of Center for Autonomous Robotic Systems.

D. Gehrig and D. Scaramuzza are with the Robotics and Perception Group, University of Zurich, Switzerland.

A. Abusafieh is with Research and Development, Strata Manufacturing PJSC (a Mubadala company), Al Ain, UAE.

Mohammed Salah is the corresponding author (email: mohammed.salah@ku.ac.ae)

noise and 2) sub-pixel localization of the calibration pattern feature points. Accordingly, this paper presents E-Calib with these attributes and the following contributions:

- 1) An efficient reweighted least squares (eRWLS) method is proposed to extract the feature points of the calibration targets in spatiotemporal domain with sub-pixel localization accuracy and robustness to noise.
- 2) A modified hierarchical clustering algorithm is devised to detect the calibration grid apart from the presence of outliers and background clutter.
- 3) We validated the proposed work in rigorous experiments for different event camera models using different calibration patterns and under challenging lighting conditions. The results show that our approach outperforms the state-of-the-art in terms of detection success rate, reprojection error, extrinsics estimation accuracy, and computational efficiency.
- 4) We release the source code of E-Calib for the community and provide an easy to use calibration toolbox for event cameras. In addition, we release ECam\_ACircles, a calibration dataset featuring calibration sequences with varying resolution, circle patterns, and lighting conditions with the ground truth pose of the camera for benchmarking of future works both available at: [https://github.com/mohammedsalah98/E\\_Calib](https://github.com/mohammedsalah98/E_Calib).

#### A. Related Work

Camera calibration recently has matured in the computer vision community with numerous algorithms have been developed to obtain the intrinsic parameters for imaging sensors [20]–[22]. Intrinsic calibration is acquired with a camera observing anchor points on a calibration pattern, where the checkerboard [23], coplanar circles [24], [25], and AprilTags [26] grids are usually utilized. For instance, conventional camera calibration became trivial and current libraries such as OpenCV [27] and MATLAB [28] provide open source calibration toolboxes.

Although image processing techniques have advanced in the past decades, the unconventional nature of event cameras inhibits the applicability of such algorithms for event-based vision. Still, knowledge of the sensor intrinsic parameters remains necessary for developing robust event-based perception algorithms. The first method developed for calibrating event cameras utilized blinking calibration patterns [16]. Since event-based vision sensors require light intensity variation to generate events, blinking screens alleviate this restriction by consistently firing events resembling checkerboard and circle calibration grids. Nonetheless, such approach needs unnecessary instrumentation as specialized screens are required to render the calibration pattern at specific frequencies [17]. More importantly, it is usually desired to move the calibration pattern instead of the event camera during calibration. This is the case when the imaging sensor is mounted on unmanned aerial and ground vehicles [29], where manipulating the blinking screen is not feasible. Due to the limitations of blinking calibration patterns, recent advances in deep learning have been utilized to reconstruct grayscale frames, where conventional calibration

methods are utilized to obtain the event camera intrinsics from the reconstructed frames. The first deep neural network to provide such utility is the E2VID network [30] where E2Calib [17] was proposed utilizing E2VID for the purpose of sensor calibration. Consequently, several improved networks have been developed: 1- Spade-E2VID by Cadena et al. [31] and 2- FireNet by Scheerlinck et al. [32]. However, the reconstructed images can suffer from artifacts as the sensor sweeps the calibration pattern degrading the feature extraction and calibration performance. This also shows that traditional image-based perception algorithms do not maximize the potential of event-based vision. Since traditional image processing techniques for event camera calibration do not provide the sufficient calibration accuracy, Huang et al. [19] proposed a multi-segment based optimization to obtain the sensor intrinsics directly from the asynchronous events using the asymmetric circle grid for its robustness against defocused scenes [33]. The aforementioned method involves utilizing density-based spatial clustering with applications of noise (DBSCAN) [34] for associating the events to their corresponding circles and each of the clustered events are utilized as control points in the multi-segment optimization framework. While the approach is the first method to propose an event-based framework for event camera calibration, it is limited by a couple of drawbacks. First, DBSCAN is performed on the spatial stamps of events and ignores their temporal dimension, leading to sub-optimal clustering performance. Second, the method utilizes the asynchronous events as the control points for the calibration optimization instead of the image centers of the circle targets. Hence, sub-pixel localization accuracy of the control points is not achieved with the edge events, which is directly correlated with degraded calibration performance. Finally, the method assumes that the clustered events corresponding to the circle targets are free from noise. However, this assumption is not valid as event-based sensors are characterized with high levels of measurement noise leading to sub-optimal calibration optimization.

#### B. Structure of The Article

The rest of the article is organized as follows. Section II provides a general overview on the proposed calibration framework. Section III outlines the events preprocessing step to assign events to their corresponding pattern circles in an unsupervised fashion. Section IV outlines the theory behind our novel feature extraction method of the calibration targets. Experimental validation of our calibration tool is provided in section V and section VI presents conclusions and future aspects of the developed work.

## II. FRAMEWORK OVERVIEW

An illustrative block diagram of our proposed calibration approach is shown in Fig. 1, involving a moving event camera observing an asymmetric circle grid. We chose the asymmetric circle grid as the calibration pattern for two reasons. First, the asymmetric circles calibration pattern is robust against out of focus scenes [33]. Second, the features generated from the circles are motion invariant, unlike checkerboards and

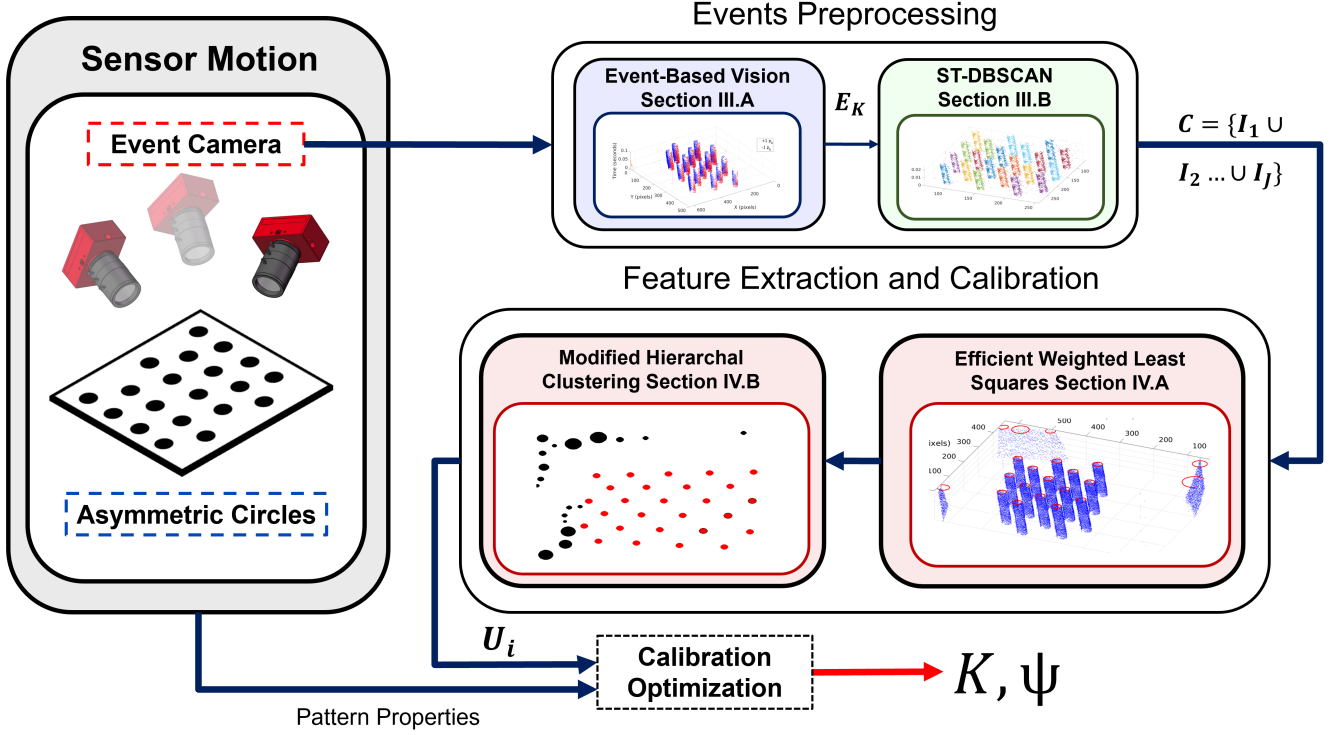


Fig. 1: A high-level block diagram of the proposed calibration method. The feature points of the pattern circles are extracted by means of efficient weighted least squares and time synchronization. The extracted centers are fed to the calibration optimization block to obtain the sensor intrinsics.

AprilTag Markers where edges parallel to camera motion do not fire events [35], see Fig. 2. As the event camera sweeps the calibration pattern of known  $M$  circles, the fired events need to be associated to their corresponding circles. Thus, we devise spatiotemporal density-based clustering with applications to noise (ST-DBSCAN) [36] to cluster the asynchronous events to their perspective circular features, outlined in section III-B. Unlike DBSCAN [34] which ignores the timestamps of the events, ST-DBSCAN performs optimal event-based clustering due to its capability to operate on spatiotemporal data and adhere to the sparse output of the event camera. It is worth mentioning that ST-DBSCAN requires predefined parameters  $\epsilon_s$  and  $\epsilon_t$ , defined as the neighborhood search radius, which require tuning for different event camera models. To circumvent this limitation, the asynchronous events are normalized with respect to the sensor resolution prior to ST-DBSCAN. This is essential to perform clustering in a unified spatiotemporal domain and ensure consistent clustering performance even for different sensor sizes.

After successfully associating the events to their perspective circles, the image centers of the calibration targets need to be extracted with sub-pixel localization accuracy to optimally calibrate the sensor. Such feature is not obtained by utilizing the raw events as control points for calibration optimization. A naive approach is to rely on ST-DBSCAN cluster centers as the feature points of the calibration targets. However, due to the inherent noisy nature of the event camera, the cluster centers drift away from the actual circle centers. Even though

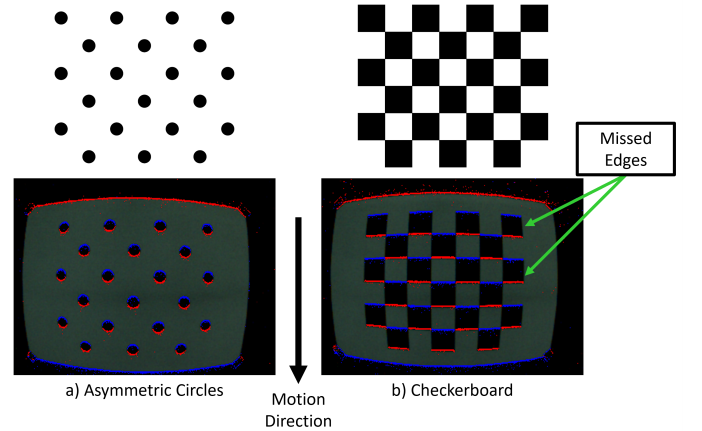


Fig. 2: Events generated for an event camera observing a) asymmetric circles pattern and b) checkerboard. Notice that the checkerboard edges parallel to camera motion do not fire events, while events for circular features are motion invariant.

ST-DBSCAN is characterized with robustness to noise, noisy events can still be mapped to the circle targets, especially when they are close to the real events. On the other hand, the observed circular features form dense slanted cylinders in spatiotemporal space due to monotonically increasing events temporal stamps, preventing the applicability of image-based feature extraction methods. To extract the image points of the pattern circles, each clustered set of events is first fed to the

efficient weighted least squares (eRWLS) algorithm, discussed in section IV-A, where cylinders are robustly fitted to the events clusters. It is essential to highlight that eRWLS assumes the probability density function (PDF) of the residual vector is dominated by a normal distribution. Accordingly, eRWLS efficiently reweights the residual vector while penalizing the outlier weights iteratively until convergence. Finally, since background clutter can be observed, a modified hierarchical clustering algorithm, detailed in section IV-B, is devised to extract the calibration pattern in the image plane apart from the background given the geometric properties of the asymmetric circle grid. As soon as the image centers are identified, they are fed to the calibration optimizer along with the pattern geometric properties to obtain the sensor intrinsic parameters.

### III. EVENTS PREPROCESSING

#### A. Event-Based Vision

The event camera is a bio-inspired technology comprising of an array of photodiode pixels triggered by log light intensity variations generating photocurrents represented by binary, asynchronous *events*. Each event is spatially and temporally stamped as

$$e_k \doteq (\mathbf{x}_k, t_k, p_k), \quad (1)$$

where  $\mathbf{x} \in Z_w \times Z_h$  is  $(x, y)_k$  defined as the pixel location,  $Z_w = \{0, 1, \dots, w-1\}$  and  $Z_h = \{0, 1, \dots, h-1\}$  with  $W$  and  $H$  represent the sensor resolution,  $t$  is the timestamp, and  $p \in \{-1, +1\}$  is the polarity of the event for a decrease and increase in the light intensity, respectively. On the other hand, even though the event camera output is dissimilar to frame-based imaging sensors, they utilize identical optics where the standard perspective projection model is followed by event cameras defined by

$$s \begin{bmatrix} u \\ v \\ 1 \end{bmatrix} = K \begin{bmatrix} R & T \end{bmatrix} \begin{bmatrix} x \\ y \\ z \\ 1 \end{bmatrix}, \quad (2)$$

where  $x, y, z$  represent the world coordinates of a point in 3D space mapped to image coordinates  $u$  and  $v$ .  $[R \ T]$  is the transformation from world coordinates to the sensor frame of reference.  $K$  is the intrinsic matrix comprising of the focal lengths  $f_x$  and  $f_y$ , and principal point  $[u_0, v_0]$ , obtained through sensor calibration. In addition to the intrinsic matrix  $K$ , lens distortion coefficients  $\Psi$  also need to be computed when calibrating event cameras defined by

$$\Psi = (k_1, k_2, p_1, p_2, k_3) \quad (3)$$

where  $(k_1, k_2, k_3)$  are the radial distortion coefficients, while  $(p_1, p_2)$  are the tangential distortion coefficients. Both  $K$  and  $\Psi$  are optimally acquired with accurate sensor calibration and are necessary for robust 3D understanding of the scene.

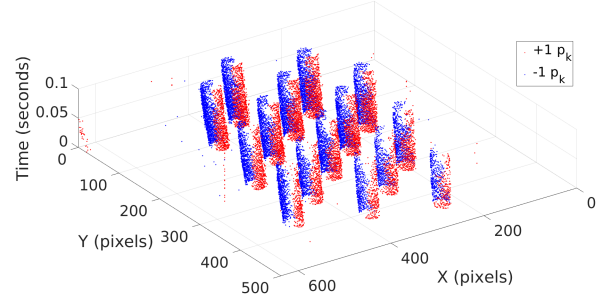


Fig. 3: Accumulated spatiotemporal window for an event camera observing the circles pattern. Notice that the circle targets form dense slanted cylinders due to the monotonic increase in time.

#### B. Unsupervised Clustering of Events

Assume that we are given a set of events  $\mathbf{E}_K$  at time  $t_K$  with elements  $e_k$  for an event camera observing the calibration grid, where  $k \in \{1, \dots, K\}$  and  $t_K > t_1$ . The events corresponding to the observed circles form dense slanted cylinders, see Fig. 3. As is the case of conventional cameras, the observed circles in the calibration pattern need to be identified from one another to calibrate the sensor, where each  $e_k$  needs to be preprocessed and associated to its corresponding circle in the calibration grid.

We utilize density-based spatiotemporal clustering of applications with noise (ST-DBSCAN) [36] algorithm to match events to their correspondent circles for to its computational efficiency and capability to adhere to the asynchronous, spatiotemporal nature of the event camera. ST-DBSCAN attempts to find dense groups of events by finding their nearest neighbors in a cylindrical region defined by the spatial radius  $\epsilon_s$  and height  $\epsilon_t$ . Accordingly, events are iteratively assigned to their clusters if their relative euclidean distance falls below  $\epsilon_s$  and  $\epsilon_t$ , otherwise they are regarded as noise. Obviously, ST-DBSCAN is more optimized to cluster events in spatiotemporal windows compared to DBSCAN, since a cylindrical search region is performed for clustering instead of the circular search area by DBSCAN.

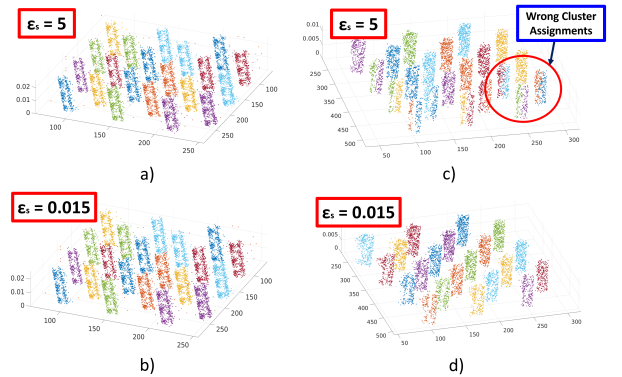


Fig. 4: a), b) and c), d) ST-DBSCAN on  $e_k$  and  $\hat{e}_k$  for DAVIS346 and DVXplorer, respectively. A fixed  $\epsilon_s$  on  $\hat{\mathbf{E}}_k$  maintains the desired clustering performance.



Intuitively,  $\epsilon_s$  is not unique when tackling different sensor sizes and calibration pattern variants of different geometric properties (i.e. height, width, and diagonal spacing). To circumvent this limitation, the spatial and temporal stamps of  $e_k \in \mathbf{E}_k$  are normalized respect to the sensor resolution ( $H \times W$ ) and the spatiotemporal window time step size  $\Delta_k$  as  $\hat{e}_k = (\frac{x}{W}, \frac{y}{H}, \frac{t_k - t_1}{\Delta_k})$ , where  $\hat{e}_k$  are the normalized events. Consequently, the input to ST-DBSCAN are the normalized events. Normalizing the events' spatial and temporal stamps makes the clustering resolution agnostic, independent of the accumulation time step size, and eventually a fixed  $\epsilon_s$  is utilized for different sensor models. Fig. 4 shows the clustering performance on  $\mathbf{E}_K$  and  $\hat{\mathbf{E}}_K$  both comprising of 4000 elements for two sensor models of different resolutions, DAVIS346 and DVXplorer. Note that the same value of  $\epsilon_s$  is identical for  $\hat{\mathbf{E}}_k$  as the events are unified under the same domain range for both sensors while ST-DBSCAN fails on raw events fails of DVXplorer.

The output of ST-DBSCAN are the sets of clustered events  $C = \{I_1, I_2, \dots, I_J\}$ , with  $\hat{\mathbf{E}}_K$  partitioned as  $\hat{\mathbf{E}}_K = I_1 \cup I_2 \cup \dots \cup I_J$ , where  $I_j \in C$  and  $J$  is the total number of clusters. In our approach, we have strictly utilized at least 4000 events to cluster  $\hat{\mathbf{E}}_K$  with a time step of 33 ms between the spatiotemporal windows. We avoided forming spatiotemporal windows based on fixed time intervals since at certain instances a very small relative motion is encountered and no sufficient features can be extracted from  $\hat{e}_k$ . On the other hand,  $\epsilon_s$  and  $\epsilon_t$  are set to 0.015 providing optimal clustering performance. It is also important to highlight that the event polarities are ignored in the clustering algorithm.

#### IV. FEATURE EXTRACTION AND CALIBRATION

##### A. Efficient Reweighted Least Squares

After obtaining the sets of clustered events  $C$ , each of the clustered sets  $\{I_1, I_2, \dots, I_J\}$  are fed to eRWLS to efficiently fit and extract the centroid of the dense cylinders formed by the observed circles grid. We first highlight the motivation of eRWLS by showing the remaining presence of outliers, where the cluster centers drift away from the true cylinder

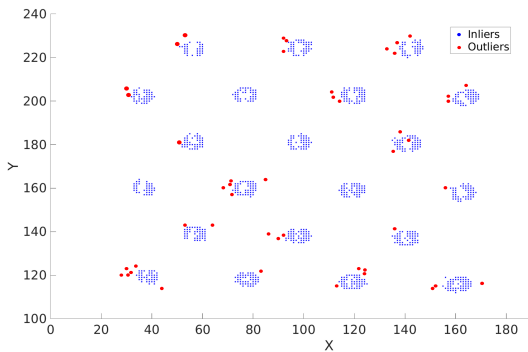


Fig. 5: The clustered events from ST-DBSCAN. Noisy events (outliers) are still evident close to the observed circle targets. Note that the figure is for illustrative purposes and events extend in the time dimension.

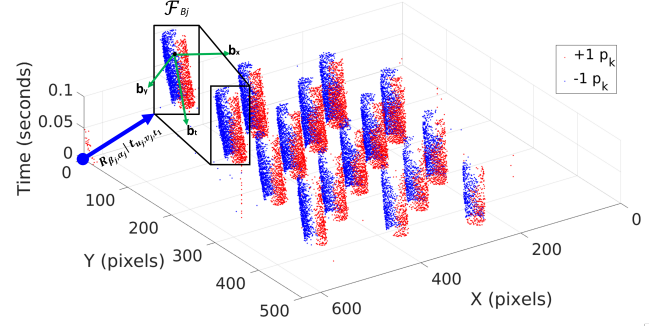


Fig. 6: The body frame  $\mathcal{F}_{Bj}$  defined for each cluster in the spatiotemporal window with the cylinder centroid defined by  $\mathbf{t}_{h,k,t}$ .

---

##### Algorithm 1 Efficient Reweighted Least Squares

---

- 1: **Inputs:**  
Clustered events sets  $C = \{I_1, I_2, \dots, I_J\}$
  - 2: **Outputs:** Cylinder parameters:  $\Omega_j$
  - 3: **Initialize:**  
 $\Omega_j = \omega_j = [\bar{r}_j, \bar{u}_j, \bar{v}_j, \beta_j = 0, \alpha_j = 0]$
  - 4: **for**  $j = 1$  to  $J$  **do**
  - 5:   **while** Not converged **do**
  - 6:     **Find**  $R_{\beta, \alpha}$  and  $\mathbf{t}_{u_j, v_j, t_{ref}}$
  - 7:     **Transform**  $e_k$  using Eq. 4
  - 8:     **Find**  $\xi$  and  $\mathbf{w}_j$ , using Eqs. 5 and 6
  - 9:     **Find**  $\sum_k w_k \xi^2$
  - 10:    **Evaluate**  $J$  and **Step**  $\Omega_j$
  - 11:    **Check** for convergence
  - 12:   **end while**
  - 13: **end for**
- 

centroid, see Fig. 5. Accordingly, eRWLS attempts to predict the desired centroids even in the presence of persisting sensor noise. Algorithm 1 defines the algorithmic procedure of eRWLS for estimating the cylinder centroids. It is also worth mentioning that the predicted centroids by eRWLS are not the actual image points to be considered for the calibration optimization. Instead, the estimated centroids are fed to the modified hierarchical clustering algorithm for detecting the circles grid before the calibration optimization.

As depicted in Fig. 3, the events for the calibration targets follow a cylinder rotated around the  $x$  the  $y$  axes of the spatiotemporal window  $\mathcal{F}_S$  with angles  $\beta_j$  and  $\alpha_j$ , respectively. We define a body frame for each of cylinder  $\mathcal{F}_{Bj}$  of basis  $[b_x, b_y, b_t]$ , where  $b_t$  resembles a monotonically increasing time dimension, see Fig. 6. Accordingly, we define the transformation,  ${}^S_S \mathcal{T}_j = [R_{\beta, \alpha} | \mathbf{t}_{u_j, v_j, t_{ref}}]$  transforming the events spatial and temporal stamps from  $\mathcal{F}_S$  to  $\mathcal{F}_{Bj}$  as

$${}^j \tilde{e}_k = \begin{bmatrix} \tilde{x}_k \\ \tilde{y}_k \\ \tilde{t}_k \end{bmatrix} = \underbrace{[R_{\beta_j, \alpha_j} | \mathbf{t}_{u_j, v_j, t_{ref}}]}_{{}^S_S \mathcal{T}_j} \begin{bmatrix} x_k \\ y_k \\ t_k \\ 1 \end{bmatrix}, \quad (4)$$

where  ${}^j \tilde{e}_k$  are the events defined in  $\mathcal{F}_{Bj}$ ,  $R_{\beta_j, \alpha_j}$  is the cylinder orientation, and  $\mathbf{t}_{u_j, v_j, t_{ref}}$  is the translation vector pointing

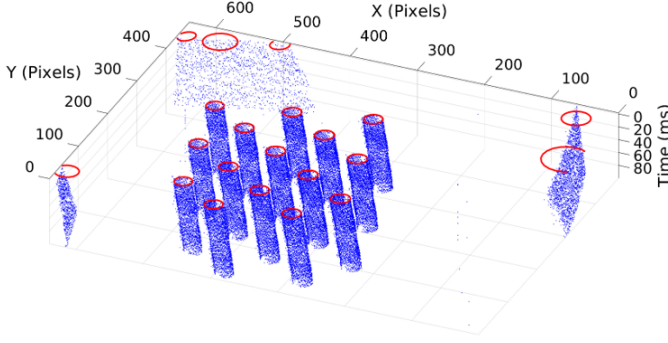


Fig. 7: Extracted cylinder centroids by eRWLS. Notice that all centroids are synchronized at  $t_{ref} = t_1$ .

from  $\mathcal{F}_S$  origin to the cylinder centroid. Note that the cylinder height is constrained at reference time  $t_{ref} = t_1$  and is not optimized. Meaning, all cylinder centroids are set to their caps at  $t_1$ , see Fig. 7. This is of paramount importance to ensure that all cylinder centroids are synchronized in time. To optimize the other the cylinder parameters,  $\Omega_j = [r_j, u_j, v_j, \beta_j, \alpha_j]$ , a nonlinear least square problem can be constructed to minimize the squared residuals  $\xi$  formulated as

$$\Omega_j^* = \arg \min_{\Omega_j} \sum_{k=1}^K \underbrace{\left( (\tilde{x}_k - u_j)^2 + (\tilde{y}_k - v_j)^2 - r_j^2 \right)}_{\xi}^2. \quad (5)$$

where  $u_j$  and  $v_j$  are the cylinder centroid, while  $r_j$  is the cylinder radius. However, the noise in event stream as shown in Fig. 5, will introduce outliers to the optimization framework which can significantly affect the optimization results. A method that provides solutions to the least squares problem that is robust against noise is the weighted least squares, but the weights for each element in the residual vector need to be provided in prior. On the other hand, iteratively reweighted least squares (IRLS) [37] can iteratively recompute the weight vector but suffers from convergence difficulties and leads to undesired computational complexities. To alleviate these restrictions, we show that the probability density function (PDF) of  $\xi$  is dominated with a Gaussian distribution and the weights  $w$  can be implicitly updated by a normally distributed vector as

$$\mathbf{w}_j = \frac{1}{\sigma\sqrt{2\pi}} e^{-(\xi\mu)^2/2\sigma^2}, \quad (6)$$

where  $\mu$  and  $\sigma$  are the mean and standard deviation of  $\zeta$ . Accordingly, the weights for the outliers are severely weakened and the cost function in Eq. 5 is modified to

$$\Omega_j^* = \arg \min_{\Omega_j} \sum_k w_k \xi^2, \quad (7)$$

where  $w_k$  are the elements of  $\mathbf{w}_j$  and Eq. 7 is iteratively minimized using the Levenberg–Marquardt algorithm [38] to compute  $\Omega_j$ . It is important to highlight that by implicitly computing  $\mathbf{w}$  of the residuals, the optimization process not only optimizes  $\Omega_j$  but inherently maximizes the likelihood of the PDF, as demonstrated in Fig. 8. Notice that at the first

iteration, the PDF is random but as the algorithm converges (i.e. iterations 5 and 8), the PDF is dominated by a normal distribution centered around  $\mu = 0$ .

One important aspect of the optimization process is the initial condition  $\omega_j$  of  $\Omega_j$ . To maintain stability and fast convergence,  $\omega_j$  is parameterized by the median of the transformed spatial stamps  $j\tilde{e}_k$  along with their norm  $\bar{r}_j$  as  $\bar{u}_j$  and  $\bar{v}_j$ , while  $\beta_j$  and  $\alpha_j$  are initialized as zeros. The optimization is run with a variable differential step computed from the jacobian  $\mathbf{J}$  [38], which has been found analytically using MATLAB symbolic toolbox [39].

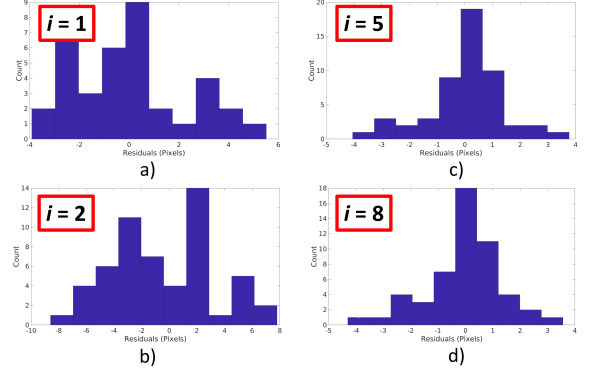


Fig. 8: The PDF for  $\xi$  at consecutive iterations. The PDF starts to slowly converge to a normal distribution progressing from a) iteration 1 to d) iteration 8.

### B. Modified Hierarchical Clustering

The synchronized cylinder centroids  $\mathbf{U}_j = [u_j, v_j]$  include the actual centers of the pattern circles in addition to false detections of the background clutter, see Fig. 7. This occurs when the sensor observes the scene background as it sweeps the calibration pattern during the data collection step. Hence, a subset of  $\mathbf{U}_j$ ,  $\mathbf{U}_i$  of  $M$  elements corresponding to the total number of pattern circles, needs to be extracted to be fed the calibration optimization. We devise a modified hierarchical clustering [40] algorithm, outlined in algorithm 2, that robustly identifies  $\mathbf{U}_i$  from  $\mathbf{U}_j$  as the desired image points for calibration optimization and the rest of the  $J - M$  centroids as outliers, where  $J > M$ .

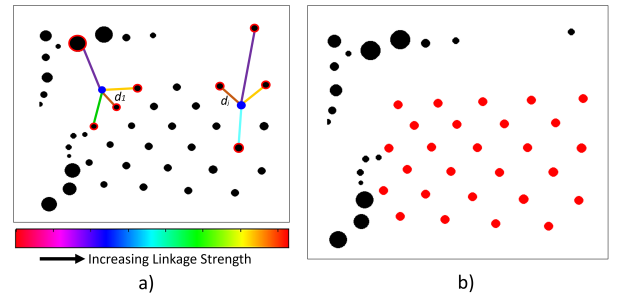


Fig. 9: a) All detected image points by the event-based circle detector with linkages formed between the clusters. b) Our modified hierarchical clustering method extracts the actual image points (red) apart from the false detections (black).

---

**Algorithm 2** Modified Hierarchical Clustering
 

---

```

1: Inputs:
    $\mathbf{U}_j = [u_j, v_j], \mathbf{r} = \{r_1, \dots, r_j\}$ 
2: Outputs: Circle Centers:  $\mathbf{U}_i$ 
3: Find linkages  $j^*, d_j$  using Eq. 8 and 9
4: Construct  $\mathbf{D} = \{d_1, \dots, d_j\}$ 
5: for  $i = 1$  to  $J C_M$  do
6:   Extract  $\mathbf{D}_\Phi, \mathbf{r}_\Phi$  with  $M$  elements using Eq. 10
7:   Find  $\varphi_i$  using Eq. 11
8:   if  $\varphi_i < \varphi_{-1}$  then
9:      $\varphi_{-1} = \varphi_i$ 
10:  end if
11: end for
  
```

---

We create a single linkage per each synchronized center to the centroid with the nearest relative euclidean distance  $d_j$  with its index as

$$j^* = \arg \min_{j'} \|(u_j, v_j) - d_{1,2,\dots,J \neq j}\|^2, \quad (8)$$

and the obtained  $j'$  is utilized to find the corresponding euclidean distance linkage as

$$d_j = \|(u_j, v_j) - (u_{j'}, v_{j'})\|^2. \quad (9)$$

This forms the set  $\mathbf{D} = \{d_1, d_2, \dots, d_J\}$  and the corresponding cylinder radii set as  $\mathbf{r} = \{r_1, r_2, \dots, r_J\}$ . Due to the uniform diagonal spacings across the circles and their identical radii, elements of  $\mathbf{D}$  and  $\mathbf{r}$  corresponding to the pattern circles are very close together compared to the background which are random and sparse, see Fig. 9. In addition, typical camera calibration procedures involve known number of pattern circles, where the maximum cluster cut-off method [40] is utilized to match the detected points to the calibration grid. The cut-off threshold is equal to  $M$  and  $\mathbf{U}_i$  corresponds to the  $M$  elements with the minimum variance of  $\mathbf{D}$  and  $\mathbf{r}$ . Therefore, the variance of all unique combinations of sets  $\mathbf{D}$  and  $\mathbf{r}$  needs to be evaluated such that the indices associated with the minimum variance correspond to  $\mathbf{U}_i$ . We define an index set  $\Phi \subset \{1, \dots, J\}$  such that  $|\Phi| = M$  used as follows

$$\mathbf{X}_\Phi = \{x_j \in \mathbf{X} \mid j \in \Phi\}. \quad (10)$$

This is also understood as extracting all unique combinations of  $M$  elements from  $\mathbf{X}$ , which will be utilized to extract subsets from  $\mathbf{D}$  and  $\mathbf{r}$ . Consequently,  $\mathbf{U}_i$  is found as

$$\mathbf{U}_i^* = \arg \min_{\Phi} \underbrace{\|\sigma(\mathbf{D}_\Phi) + \sigma(\mathbf{r}_\Phi)\|}_{\varphi} \quad (11)$$

where  $\sigma$  is the standard deviation of the set. Note that Eq. 11 is evaluated  $J C_M$  times and  $\mathbf{U}_i$  is identified with index set  $\Phi$  that corresponds to the minimum joint variance norm  $\varphi$  of  $\mathbf{D}$  and  $\mathbf{r}$ .

Once  $\mathbf{U}_i$  is identified for sufficient number of pattern detections  $N$ , it is utilized as the control points for the calibration optimization, where the estimated parameters are the intrinsic

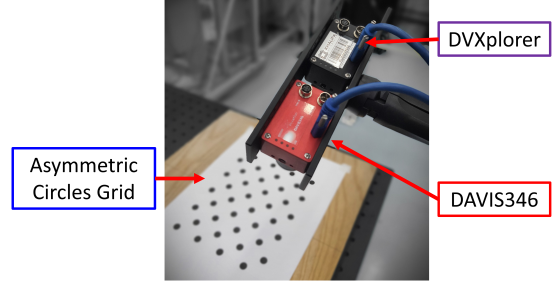


Fig. 10: Experimental setup for validating the proposed calibration algorithm for event camera variants observing an asymmetric circles calibration pattern.

matrix  $K$  and the distortion coefficients  $\Psi$ . Given their initial guess,  $\mathbf{U}_i$  is shifted by the radial distortion coefficients as

$$x_i = x_r(1 + k_1 r^2 + k_2 r^4 + k_3 r^6) \quad (12)$$

$$y_i = y_r(1 + k_1 r^2 + k_2 r^4 + k_3 r^6). \quad (13)$$

where  $(x_i, y_i) = (u_i - u_0, v_i - v_0)$  and  $r = \sqrt{x_i^2 + y_i^2}$ , with  $[u_0, v_0]$  being the principal point. Consequently, the tangential distortion is accounted for by

$$x_r = x_{r,t} + [2p_1 x_{r,t} y_{r,t} + p_2(r^2 + 2x_{r,t}^2)] \quad (14)$$

$$y_r = y_{r,t} + [p_1(r^2 + 2y_{r,t}^2) + 2p_2 x_{r,t} y_{r,t}]. \quad (15)$$

The undistorted points,  $u_{r,t} = x_{r,t} + u_0, v_{r,t} = y_{r,t} + v_0$  form the undistorted image points vector  $\mathbf{U}_{r,t}$  and the camera parameters are obtained by minimizing the reprojection error as

$$K^*, \Psi^* = \arg \min_{K, \Psi} \sum_{n=1}^N \sum_{i=1}^M \|\mathbf{U}_{r,t} - \pi(K, {}^P\mathbf{U}, {}^P_C\mathcal{T})\|^2, \quad (16)$$

where  $N$  is the total number of pattern detections,  $M$  is the total number of circles in the calibration pattern,  ${}^P\mathbf{U}$  are the coordinates of the calibration targets defined in the pattern reference frame, and  $\pi$  is the projection of  ${}^P\mathbf{U}$  into the event camera frame, which is obtained by the camera projection matrix [41]. Eq. 16 is minimized by the levenberg-Marquardt algorithm to obtain  $K$  and  $\Psi$  [41].

## V. EXPERIMENTS

### A. Experimental Setup

We have tested the proposed algorithm in various challenging scenarios demonstrated in our ECam\_ACircles dataset. To show that our proposed approach is resolution agnostic, event camera models with different resolutions were calibrated by the devised algorithm; the DAVIS346 ( $346 \times 260$ ) and DVXplorer ( $640 \times 480$ ), see Fig. 10. Both cameras are interfaced with robot operating system (ROS) using a USB 3.0 terminal on the host computer. We have also tested our method on three calibration pattern variants of ECam\_ACircles, of dimensions  $3 \times 7$  and  $34$  mm diagonal spacing,  $3 \times 9$  and  $27$  mm diagonal

TABLE I: Detection success rate and reprojection error on the ECam\_ACircles dataset. Notice that high detection success rates and low reprojection errors are maintained even at challenging lighting conditions demonstrating robustness against noise.

Metric	Dataset								
	<i>davis_3x7_gdlight</i>	<i>davis_3x7_lowlight</i>	<i>davis_3x9_gdlight</i>	<i>davis_3x9_lowlight</i>	<i>davis_4x11_gdlight</i>	<i>davis_4x11_lowlight</i>	<i>dvx_3x7_gdlight</i>	<i>dvx_3x9_gdlight</i>	<i>dvx_4x11_gdlight</i>
Data Sequence Time (s)	17.04	15.37	27.02	24.04	19.07	18.53	15.53	27.04	14.99
Total Detections	438	362	709	648	437	392	330	672	312
Detection Success Rate (%)	84.12	80.44	90.89	89.99	76.84	71.68	72.34	82.98	74.44
$\zeta_r$ (Px)	0.13	0.19	0.13	0.17	0.16	0.21	0.46	0.51	0.43

spacing, and  $4 \times 11$  and 24 mm diagonal spacing. This is of paramount importance to prove that the developed calibration framework successfully calibrates event cameras regardless of the pattern geometric properties. Finally, the work of the paper was assessed in good (93.21 Lux) and poorly lit environments (8.72 Lux) to demonstrate robustness against illumination variation and increasing noise with degraded lighting conditions. Videos of the experiments are available through the following link: <https://youtu.be/4giQn6rt-48>.

We evaluated our method on the aforementioned experiments based on three metrics: 1) Detection success rate, 2) calibration reprojection error, and 3) positioning error of the estimated extrinsics. While comparing the calibration reprojection error and the obtained intrinsics to the DAVIS346 frames can be sufficient for validation, inaccurate intrinsics can be obtained as the solver can converge to a local minimum, even though a low reprojection error is achieved. This is usually witnessed with the lens distortion coefficients. Thus, we additionally compare the calibrated extrinsics to the ground truth pose of the camera, which is provided by OptiTrack Prime 13 motion capture system to further evaluate our method fairly. It is worth mentioning that the positioning measurements from OptiTrack and the estimated extrinsics are synchronized using soft time synchronization [42].

### B. Calibration Accuracy Evaluation

To obtain optimal intrinsics of the event camera, 1) sufficient number of detections of the asymmetric circle grid is required and 2) the detected circle centers need to be localized with sub-pixel accuracy in the image plane. Accordingly, we compare our eRWLS feature extraction method to the detection performance of MATLAB's state-of-the-art detector, *detectCircleGridPoints* [43], applied on the frames of the DAVIS APS sensor and MR algorithm for *davis\_4x11\_gdlight* and *dvx\_4x11\_dataset* datasets, demonstrated in Fig. 11. In addition, the detection success rate evaluates the performance of our modified hierarchical clustering algorithm to detect the circle grid even in the presence of scene background. *detectCircleGridPoints* fails to detect the calibration pattern on the DAVIS frames due to the fact that motion blur is witnessed and the features of the calibration grid are degraded. On the other hand, even though the MR frames suffer from noise and artifacts significantly degrading the image quality and the calibration grid is not extracted.

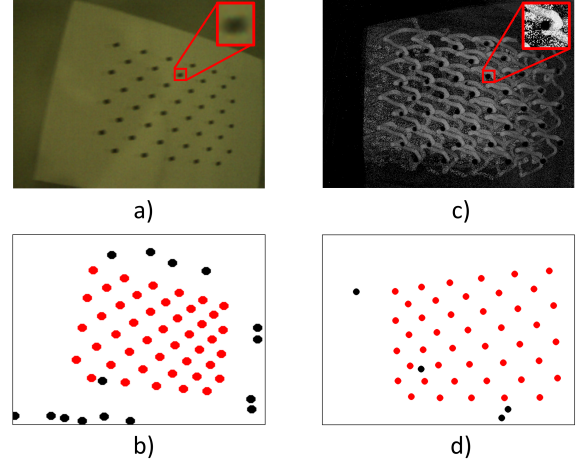


Fig. 11: Asymmetric circle grid detected using [43] on a) DAVIS and c) DVXplorer MR frame, while b) and d) represent our approach detecting a  $4 \times 11$  grid.

To the contrary, our calibration tool, leveraging the asynchronous nature of events, detects the calibration pattern even when high speed motion is induced. We first evaluate the proposed calibration approach in terms of the detection success rate on ECam\_ACircles dataset to ensure that calibration is attainable, where the detection success rate is defined as the fraction of times the pattern was detected against the total

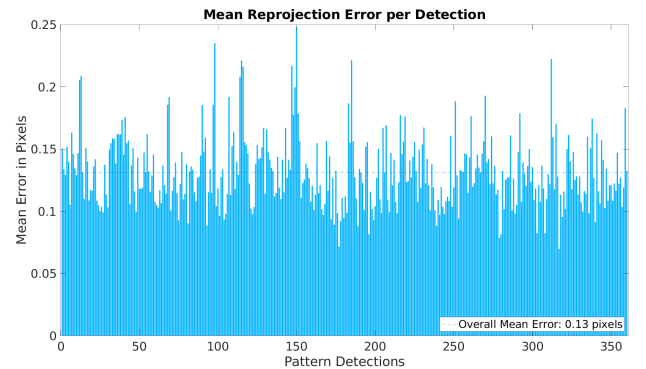


Fig. 12: Reprojection errors on *davis\_3x9\_gdlight* dataset where  $\zeta_r = 0.13$  pixels was obtained.



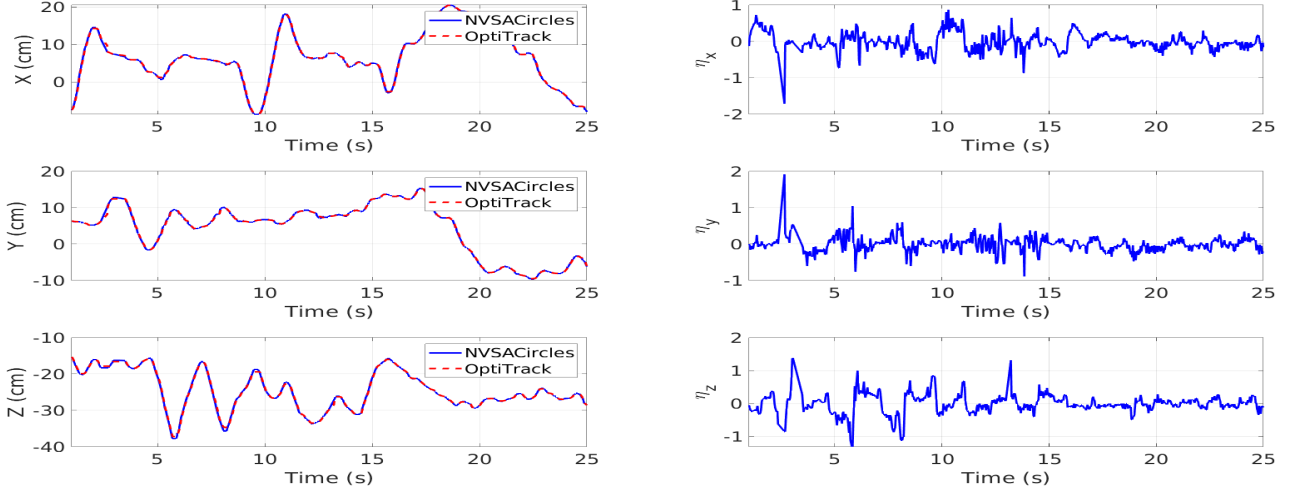


Fig. 13: Pose estimates by our method compared against ground truth pose of the camera from the motion capture system. Our approach achieves a mean absolute positioning error  $\hat{\eta}_t$  of 0.952 cm and maximum positioning error  $\eta_t^{max}$  of 1.72 cm.

number of detections that can be obtained. It is worth noting that the total number of detections of the calibration pattern is equal to the data sequence time divided by the time step between the spatiotemporal windows, which we have defined as 33 ms. The detection success rates are shown in Table I. Notice that the detection success rate is high for both sensors showing that our approach proves to be resolution agnostic. In addition, the detection success rate is maintained even at challenging illumination conditions demonstrating that the proposed eRWLS is robust against noise and the modified hierarchical clustering algorithm identifies the calibration pattern despite the presence of the noisy background.

Having a sufficient number of pattern detections, the calibration accuracy is mainly dependent on the feature extraction performance of eRWLS since a state-of-the-art calibration optimization is utilized to obtain the sensor parameters. Hence, the calibration performance is evaluated in terms of the reprojection error and the deviation of the obtained intrinsic parameters from the conventional frames. The reprojection errors  $\zeta_r$ , evaluated similar to [41], are reported in Table I and Fig. 12, while the obtained intrinsics compared against the conventional frames is reported in Table II. Note that this comparison is only applicable on *davis\_3x9\_gdlight* because calibration was only successful using the DAVIS frames on the aforementioned dataset due to the slow sensor motion and adequate lighting conditions. The obtained results show that eRWLS extracts the pattern circle centers with the required accuracy. Moreover, low reprojection errors are maintained even in poorly illuminated environments, where sensor noise drastically increases. This shows the importance of time synchronization of the predicted circle centers for maintaining optimal calibration performance.

### C. Pose Estimation Results

While in most cases the calibration reprojection error can serve as a good benchmark for our method, in some occasions calibration can converge to a local minimum with

TABLE II: The obtained intrinsics of the event camera by our method are compared against the parameters acquired by the DAVIS frames on *davis\_3x9\_gdlight*.

Metric	Frames	Ours
$\zeta_r$ (Px)	0.11	0.13
$f_x, f_y$ (Px)	355.35, 354.31	355.54, 353.97
$u_0, v_0$	159.84, 126.63	159.16, 124.45
$k_1, k_2, k_3$	-0.3469, 0.122, 0.1921	-0.333, 0.075, 0.271
$p_1, p_2$	-0.000598, -0.000513	-0.000670, -0.000596
Detection Success Rate (%)	79.92	84.12

the reprojection error being relatively low but the obtained sensor parameters are not optimal. Thus, we also validate the proposed method in terms of the estimated extrinsics. The estimated camera pose by our method is compared to the sensor ground truth pose given by the OptiTrack motion capture system in terms of the mean absolute error. The results are reported in Table III on ECam\_ACircles dataset in terms of the mean absolute translation  $\hat{\eta}_t$  and rotation errors  $\hat{\eta}_r$ , and their corresponding standard deviations  $\sigma_t$  and  $\sigma_r$ . Fig. 13 also shows the positioning plots compared against the OptiTrack for *davis\_3x9\_gdlight*.

Accurate pose estimation is directly correlated with robust tracking of the calibration targets centers. If ST-DBSCAN cluster centers are utilized as circle centers,  $\zeta_r$  grows to 0.44 pixels and  $\hat{\eta}_t$  rises to 6.71 cm on *davis\_3x9\_gdlight*. This demonstrates the need for eRWLS refinement since ST-DBSCAN cluster centers are affected by severe sensor noise, especially in challenging lighting conditions. In addition, our method provides accurate estimates of the sensor pose and maintains a pose estimation error in poorly lighted environments of the same order of magnitude compared to data sequences collected at good lighting conditions. This shows robustness against the event camera noise, which increases with decreasing illumination.



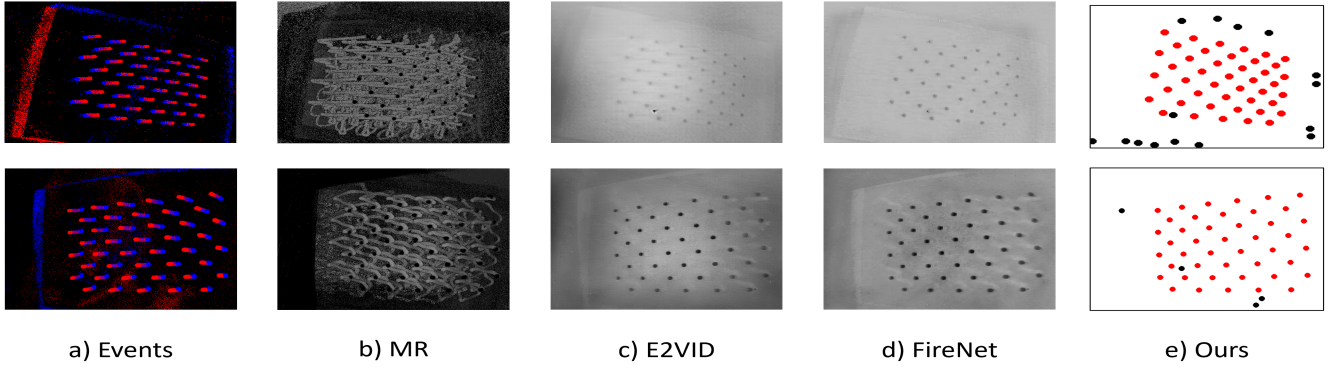


Fig. 14: Data sequences on the *davis\_4x11\_gdlight* (top) and *dvx\_4x11\_dataset* (bottom), where state-of-the-art methods fail to detect the calibration pattern, while our method robustly detects the asymmetric circle grid.

TABLE III: Detection success rate and reprojection error on the ECam\_ACircles dataset. Notice that high detection success rates and low reprojection errors are maintained even at challenging lighting conditions demonstrating robustness against noise.

Metric	Dataset								
	<i>davis_3x7_gdlight</i>	<i>davis_3x7_lowlight</i>	<i>davis_3x9_gdlight</i>	<i>davis_3x9_lowlight</i>	<i>davis_4x11_gdlight</i>	<i>davis_4x11_lowlight</i>	<i>dvx_3x7_gdlight</i>	<i>dvx_3x9_gdlight</i>	<i>dvx_4x11_gdlight</i>
$\hat{\eta}_t$ (cm)	0.480	1.190	0.952	0.721	0.786	0.947	0.370	1.048	0.510
$\sigma_t$ (cm)	0.0319	0.079	0.083	0.0751	0.0506	0.0686	0.0851	0.0459	0.0606
$\hat{\eta}_r$ (°)	0.7730	1.4964	0.8290	0.6970	0.7362	1.0491	0.8981	0.9367	0.3711
$\sigma_r$ (°)	0.0347	0.0436	0.0435	0.0312	0.0284	0.0504	0.0573	0.0497	0.0219

TABLE IV: The proposed event-based calibration algorithm is benchmarked against the works of Reinbacher et al [44], Muglikar et al. [17], Scheerlinck et al. [32] and Huang et al. [19] on the *davis\_3x9\_gdlight*. The dash indicates the metric is not applicable while † represents failure of obtaining the parameter.

Algorithm	DAVIS Frames	Reinbacher et al. [44]	Muglikar et al. [17]	Scheerlinck et al. [32]	Huang et al. [19]	Ours
Year	-	2016	2019	2020	2021	2023
Reprojection Error $\zeta_r$	0.11	†	0.13	0.19	0.29	<b>0.13</b>
Focal Length ( $f$ )	355.35	†	372.28	360.71	357.091	<b>355.54</b>
$k_1, k_2, k_3$	-0.344, 0.117, -0.0178	†	-0.081, 0.199, -0.313	-0.291, 0.0367, -0.112	-0.359, 0.396, -0.7178	<b>-0.339, 0.071, -0.0271</b>
$u_0, v_0$	159.84, 125.63	†	164.23, 129.78	163.11, 128.24	158.98, 124.39	<b>159.16, 124.45</b>
Pattern Detections	345	3	41	62	-	<b>709</b>
Detection Success Rate	79.99%	0.38%	9.51%	13.91%	-	<b>84.12</b>

#### D. Benchmarks

To evaluate the impact of our event-driven calibration tool, we compare our results to state-of-the-art methods that include E2VID network by Muglikar et al. [17], FireNet by Scheerlinck et al. [32], and the MR approach by Reinbacher et al. [44]. The methods are compared to the work of this paper in terms of the detection success rate, reprojection error, and pose error if calibration was successful by a designated method. Fig. 14 compares the detection performance of our method against the aforementioned works. An important point is that detection success rate was not evaluated on the work of Huang et al. [19] since the required number of pattern detections is preset before running calibration. We have set this value to 700 sufficient to perform proper calibration, to compare the obtained results fairly and such that the total number of pattern detections are within the same order of magnitude. Table IV lists our results compared to those works on the *davis\_3x9\_gdlight* dataset. In addition, only the radial distortion were computed for the

benchmarks, while tangential distortion was ignored for all methods since it is not computed by Huang et al. [19]. It is also worth mentioning that these approaches were tested on the *davis\_3x9\_gdlight* by the codes publicly available by the authors of these papers.

Our approach outperforms the state-of-the-art significantly in terms of reprojection error, detection success rate, and intrinsic parameters values. The manifold regularization method by Muglikar et al. [44] failed to calibrate the camera and detect the calibration grid due to artifacts and sensor noise present in the reconstructed images. On the other hand, calibration was attained using E2VID [17] and FireNet [32], but the intrinsics deviate away from the parameters obtained by the frames as the calibration converged to a local minimum, even though a low reprojection error is obtained. This occurred because most of the pattern detections were redundant and the calibration grid was not sufficiently detected from multiple views due to the degraded features of the circles in the reconstructed images, see Fig. 14. Note that MATLAB's *detectCircleGrid*

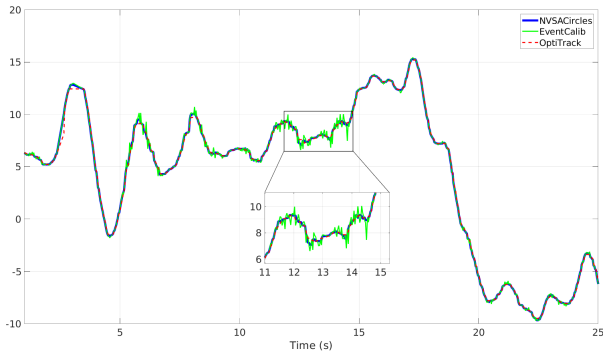


Fig. 15: Camera pose estimate plot along the Y-axis of our method, the work of Huang et al. [19], and ground truth from OptiTrack. Notice the pose estimates are smoother due to our improved method of tracking the circular features.

*Points* [43] was utilized to extract the calibration grid from the reconstructed images. Finally, calibration was successful by Huang et al. [19] method. Yet, our approach provides improved calibration accuracy also in terms of reprojection error and the intrinsics. Even though the obtained focal length by Huang’s method is close to the focal length obtained by the DAVIS frames, the radial distortion coefficients deviate from their true values. This is because the aforementioned approach relies on the raw events as control points, where sub-pixel localization of the circle centers is not attained leading to sub-optimal calibration accuracy.

In addition to the intrinsic parameters, the obtained extrinsics were also validated against the ground truth pose of the camera and compared to the camera pose estimation results by our method, Huang’s method, E2VID, and FireNet. Fig. 15 shows the positioning plot on *davis\_3x9\_gdlight* along the y-axis and Table V quantifies these results with the same metrics reported in Table III. Table V also reports the positioning results of E2VID and FireNet, where a large positioning error was obtained due to the sub-optimal intrinsic parameters. On the other hand, Huang’s method and our approach provide satisfactory results in terms of a mean positioning error. However, our calibration tool shows a smoother estimate of camera trajectory, demonstrating the capability of our method to provide more optimal sensor intrinsics. This occurred due to the sub-optimal optimization of the lens distortion coefficients and illustrates that sub-pixel localization accuracy of the circle centers is necessary for optimal sensor calibration, which is attained by our method unlike Huang’s approach.

TABLE V: Mean absolute pose error by our method and the works of Muglikar et al. [17], Scheerlinck et al. [32], and Huang et al. [19] compared against ground truth camera pose obtained from OptiTrack.

Method	Huang et al.	Muglikar et al.	Scheerlinck et al.	Ours
$\hat{\eta}_t$ (cm)	1.97	4.49	3.95	<b>0.952</b>
$\hat{\sigma}_t$ (cm)	0.129	0.396	0.218	<b>0.083</b>
$\eta_t^{max}$ (cm)	3.18	8.14	7.69	<b>1.72</b>
$\hat{\eta}_r$ (°)	2.31	5.37	4.99	<b>0.8290</b>
$\hat{\sigma}_r$ (°)	0.0913	0.271	0.179	<b>0.0435</b>
$\eta_r^{max}$ (°)	3.17	9.77	8.56	<b>1.13</b>

The average execution time of the proposed work for datasets on the DAVIS346 and DVXplorer is also reported for each algorithm block, see Table VI. Compared to E2VID and FireNet networks, which run offline and require GPU acceleration, our algorithm outperforms these approaches in execution time without the need for heavy computational resources. On the other hand, while the MR approach achieves real-time performance, it suffers in terms of feature extraction performance and detection success rate. Nevertheless, our approach can surely be utilized for online calibration of the sensor. In addition, real-time performance is unnecessary for intrinsic calibration as redundant frames can be captured in close time steps. Nevertheless, it is worth mentioning that our algorithm is written on Python and MATLAB and was executed on Ryzen 7 6800H (3.2 GHz) processor. Thus, our execution time can be further improved if implemented using C++, especially if execution in real-time is needed.

TABLE VI: Execution times for the system blocks.

Algorithm	DAVIS346 (s)	DVXplorer (s)
ST-DBSCAN	0.043	0.067
Efficient Reweighted Least Squares	0.016	0.029
Modified Hierarchical Clustering	0.0012	0.0014
<b>Total</b>	<b>0.0602</b>	<b>0.0974</b>

## VI. CONCLUSION

In this paper, a robust calibration tool is proposed for obtaining the intrinsic parameters of event cameras. Without relying on conventional image processing techniques, the demonstrated approach leverages the asynchronous nature and low latency of the event camera to provide robust estimates of the sensor intrinsics. This was attained by a resolution agnostic density-based spatiotemporal clustering algorithm. More importantly, a novel and efficient reweighted least squares (eRWLS) method was proposed to extract the features of the calibration targets despite the presence of sensor noise. The robustness and ability of eRWLS to track the circular features with sub-pixel accuracy played an important role in acquiring the desired calibration accuracy and outperforming state-of-the-art methods for event cameras calibration. In addition, our calibration tool introduced a modified hierarchical clustering algorithm to detect the calibration grid even in the presence of background clutter. The proposed method was tested in a variety of rigorous experiments on different sensor models, circle grids of different geometric properties, and under challenging illumination environments. The experiments demonstrated that our method outperformed the state of the art in terms of detection success rate, reprojection, and pose error. While the proposed work was utilized for calibrating event cameras, it can be utilized for event-based circle detection, a fundamental exigency in robot perception algorithms. Future work will also extend this work for calibrating stereo event cameras and extrinsic calibration of event cameras in robotic systems.

## REFERENCES

- [1] G. Gallego, T. Delbrück, G. Orchard, C. Bartolozzi, B. Taba, A. Censi, S. Leutenegger, A. J. Davison, J. Conradt, K. Daniilidis, and D. Scara-

- muzza, "Event-based vision: A survey," *IEEE Transactions on Pattern Analysis and Machine Intelligence*, vol. 44, no. 1, pp. 154–180, 2022.
- [2] Y. Alkendi, R. Azzam, A. Ayyad, S. Javed, L. Seneviratne, and Y. Zweiri, "Neuromorphic camera denoising using graph neural network-driven transformers," *IEEE Transactions on Neural Networks and Learning Systems*, pp. 1–15, 2022.
  - [3] P. Lichtsteiner, C. Posch, and T. Delbruck, "A  $128 \times 128$  120 db 15  $\mu$ s latency asynchronous temporal contrast vision sensor," *IEEE Journal of Solid-State Circuits*, vol. 43, no. 2, pp. 566–576, 2008.
  - [4] M. Salah, M. Chehadah, M. Humais, M. Wabbah, A. Ayyad, R. Azzam, L. Seneviratne, and Y. Zweiri, "A neuromorphic vision-based measurement for robust relative localization in future space exploration missions," *IEEE Transactions on Instrumentation and Measurement*, pp. 1–1, 2022.
  - [5] F. Mählknecht, D. Gehrig, J. Nash, F. M. Rockenbauer, B. Morrell, J. Delaune, and D. Scaramuzza, "Exploring event camera-based odometry for planetary robots," *IEEE Robotics and Automation Letters*, vol. 7, no. 4, pp. 8651–8658, 2022.
  - [6] S. Roffe, H. Akolkar, A. D. George, B. Linares-Barranco, and R. B. Benosman, "Neutron-induced, single-event effects on neuromorphic event-based vision sensor: A first step and tools to space applications," *IEEE Access*, vol. 9, pp. 85 748–85 763, 2021.
  - [7] A. Ayyad, M. Halwani, D. Swart, R. Muthusamy, F. Almaskari, and Y. Zweiri, "Neuromorphic vision based control for the precise positioning of robotic drilling systems," *Robotics and Computer-Integrated Manufacturing*, vol. 79, p. 102419, 2023. [Online]. Available: <https://www.sciencedirect.com/science/article/pii/S0736584522001041>
  - [8] J. Li, J. Li, L. Zhu, X. Xiang, T. Huang, and Y. Tian, "Asynchronous spatio-temporal memory network for continuous event-based object detection," *IEEE Transactions on Image Processing*, vol. 31, pp. 2975–2987, 2022.
  - [9] Y. Zheng, Z. Yu, S. Wang, and T. Huang, "Spike-based motion estimation for object tracking through bio-inspired unsupervised learning," *IEEE Transactions on Image Processing*, vol. 32, pp. 335–349, 2023.
  - [10] M. Gehrig and D. Scaramuzza, "Recurrent vision transformers for object detection with event cameras," in *Proceedings of the IEEE/CVF Conference on Computer Vision and Pattern Recognition (CVPR)*, June 2023, pp. 13 884–13 893.
  - [11] N. Messikommer, C. Fang, M. Gehrig, and D. Scaramuzza, "Data-driven feature tracking for event cameras," in *Proceedings of the IEEE/CVF Conference on Computer Vision and Pattern Recognition (CVPR)*, June 2023, pp. 5642–5651.
  - [12] J. Bertrand, A. Yiğit, and S. Durand, "Embedded event-based visual odometry," in *2020 6th International Conference on Event-Based Control, Communication, and Signal Processing (EBCCSP)*, 2020, pp. 1–8.
  - [13] D. Falanga, K. Kleber, and D. Scaramuzza, "Dynamic obstacle avoidance for quadrotors with event cameras," *Science Robotics*, vol. 5, no. 40, p. eaaz9712, 2020. [Online]. Available: <https://www.science.org/doi/abs/10.1126/scirobotics.aaz9712>
  - [14] S. Sun, G. Cioffi, C. de Visser, and D. Scaramuzza, "Autonomous quadrotor flight despite rotor failure with onboard vision sensors: Frames vs. events," *IEEE Robotics and Automation Letters*, vol. 6, no. 2, pp. 580–587, apr 2021. [Online]. Available: <https://doi.org/10.1109%2Fflra.2020.3048875>
  - [15] G. Chen, W. Chen, Q. Yang, Z. Xu, L. Yang, J. Conradt, and A. Knoll, "A novel visible light positioning system with event-based neuromorphic vision sensor," *IEEE Sensors Journal*, vol. 20, no. 17, pp. 10 211–10 219, 2020.
  - [16] G. Orchard, "Dvscalibration," 2016. [Online]. Available: <https://github.com/gorchard/DVScalibration>
  - [17] M. Muglikar, M. Gehrig, D. Gehrig, and D. Scaramuzza, "How to calibrate your event camera," in *2021 IEEE/CVF Conference on Computer Vision and Pattern Recognition Workshops (CVPRW)*, 2021, pp. 1403–1409.
  - [18] C. Brandli, R. Berner, M. Yang, S.-C. Liu, and T. Delbruck, "A  $240 \times 180$  130 db 3  $\mu$ s latency global shutter spatiotemporal vision sensor," *IEEE Journal of Solid-State Circuits*, vol. 49, no. 10, pp. 2333–2341, 2014.
  - [19] K. Huang, Y. Wang, and L. Kneip, "Dynamic event camera calibration," in *2021 IEEE/RSJ International Conference on Intelligent Robots and Systems (IROS)*, 2021, pp. 7021–7028.
  - [20] C. Ricolfe-Viala and A. Esparza, "The influence of autofocus lenses in the camera calibration process," *IEEE Transactions on Instrumentation and Measurement*, vol. 70, pp. 1–15, 2021.
  - [21] J.-H. Chuang, C.-H. Ho, A. Umam, H.-Y. Chen, J.-N. Hwang, and T.-A. Chen, "Geometry-based camera calibration using closed-form solution of principal line," *IEEE Transactions on Image Processing*, vol. 30, pp. 2599–2610, 2021.
  - [22] S.-E. Lee, K. Shibata, S. Nonaka, S. Nobuhara, and K. Nishino, "Extrinsic camera calibration from a moving person," *IEEE Robotics and Automation Letters*, vol. 7, no. 4, pp. 10 344–10 351, 2022.
  - [23] C. Yu and Q. Peng, "Robust recognition of checkerboard pattern for camera calibration," *Optical Engineering - OPT ENG*, vol. 45, 09 2006.
  - [24] F. Bergamasco, L. Cosmo, A. Albarelli, and A. Torsello, "Camera calibration from coplanar circles," *Proceedings - International Conference on Pattern Recognition*, pp. 2137–2142, 12 2014.
  - [25] K.-Y. K. Wong, G. Zhang, and Z. Chen, "A stratified approach for camera calibration using spheres," *IEEE Transactions on Image Processing*, vol. 20, no. 2, pp. 305–316, 2011.
  - [26] E. Olson, "Apriltag: A robust and flexible visual fiducial system," in *2011 IEEE International Conference on Robotics and Automation*, 2011, pp. 3400–3407.
  - [27] A. Bradski, *Learning OpenCV, Computer Vision with OpenCV Library software that sees*, 1st ed. O'Reilly Media, 2008, gary Bradski and Adrian Kaehler.
  - [28] J. Bouguet, "Matlab camera calibration toolbox," 2000.
  - [29] J. Harguess and S. Strange, "Infrared stereo calibration for unmanned ground vehicle navigation," in *Proceedings of SPIE - The International Society for Optical Engineering*, vol. 9084, 06 2014, p. 90840S.
  - [30] H. Rebecq, R. Ranftl, V. Koltun, and D. Scaramuzza, "High speed and high dynamic range video with an event camera," *IEEE Transactions on Pattern Analysis and Machine Intelligence*, vol. 43, no. 6, pp. 1964–1980, 2021.
  - [31] P. R. G. Cadena, Y. Qian, C. Wang, and M. Yang, "Spade-e2vid: Spatially-adaptive denormalization for event-based video reconstruction," *IEEE Transactions on Image Processing*, vol. 30, pp. 2488–2500, 2021.
  - [32] C. Scheerlinck, H. Rebecq, D. Gehrig, N. Barnes, R. Mahony, and D. Scaramuzza, "Fast image reconstruction with an event camera," in *IEEE Winter Conf. Appl. Comput. Vis. (WACV)*, 2020, pp. 156–163.
  - [33] K. S. Rattan, D. Ph., T. Wischgoll, and R. E. W. Fyffe, "A comparison of monocular camera calibration techniques," 2014.
  - [34] M. Ester, H.-P. Kriegel, J. Sander, and X. Xu, "A density-based algorithm for discovering clusters in large spatial databases with noise," ser. KDD'96. AAAI Press, 1996, p. 226–231.
  - [35] R. Muthusamy, A. Ayyad, M. Halwani, D. Swart, D. Gan, L. Seneviratne, and Y. Zweiri, "Neuromorphic eye-in-hand visual servoing," *IEEE Access*, vol. 9, pp. 55 853–55 870, 2021.
  - [36] D. Birant and A. Kut, "ST-DBSCAN: An algorithm for clustering spatial-temporal data," *Data & Knowledge Engineering*, vol. 60, no. 1, pp. 208–221, 2007, intelligent Data Mining. [Online]. Available: <https://www.sciencedirect.com/science/article/pii/S0169023X06000218>
  - [37] P. J. Green, "Iteratively reweighted least squares for maximum likelihood estimation, and some robust and resistant alternatives," *Journal of the Royal Statistical Society. Series B (Methodological)*, vol. 46, no. 2, pp. 149–192, 1984. [Online]. Available: <http://www.jstor.org/stable/2345503>
  - [38] K. Levenberg, "A method for the solution of certain non-linear problems in least squares," *Quarterly of Applied Mathematics*, vol. 2, no. 2, pp. 164–168, 1944. [Online]. Available: <http://www.jstor.org/stable/43633451>
  - [39] I. The MathWorks, *Symbolic Math Toolbox*, Natick, Massachusetts, United States, 2019. [Online]. Available: <https://www.mathworks.com/help/symbolic/>
  - [40] S. Patel, S. Sihmar, and A. Jatain, "A study of hierarchical clustering algorithms," in *2015 2nd International Conference on Computing for Sustainable Global Development (INDIACom)*, 2015, pp. 537–541.
  - [41] Z. Zhang, "A flexible new technique for camera calibration," *IEEE Transactions on Pattern Analysis and Machine Intelligence*, vol. 22, no. 11, pp. 1330–1334, 2000.
  - [42] h. Hu, J. Wu, and Z. Xiong, "A soft time synchronization framework for multi-sensors in autonomous localization and navigation," in *2018 IEEE/ASME International Conference on Advanced Intelligent Mechatronics (AIM)*, 2018, pp. 694–699.
  - [43] MATLAB. Detect circle grid pattern in images. [Online]. Available: <https://www.mathworks.com/help/vision/ref/detectcirclegridpoints.html>
  - [44] G. Munda, C. Reinbacher, and T. Pock, "Real-time intensity-image reconstruction for event cameras using manifold regularisation," *International Journal of Computer Vision*, vol. 126, no. 12, pp. 1381–1393, Jul. 2018.



**Mohammed Salah** received his BSc. in Mechanical Engineering from American University of Sharjah, UAE, in 2020 and his MSc. in Mechanical Engineering from Khalifa University, Abu Dhabi, UAE, in 2022. He is currently with Khalifa University Center for Autonomous Robotic Systems (KUCARS). His research interest is mainly focused on multi-sensor fusion, neuromorphic vision, and space robotics.



**Abdulla Ayyad** (Member, IEEE) received the M.Sc. degree in electrical engineering from The University of Tokyo, in 2019, where he conducted research with the Spacecraft Control and Robotics Laboratory. He is currently a Research Associate at the Advanced Research and Innovation Center (ARIC) at Khalifa University working on several robot autonomy projects. His current research interest includes the application of AI in the fields of perception, navigation, and control.



**Muhammad Humais** received his M.Sc. in Electrical and Computer Engineering from Khalifa University in 2020. His research is mainly focused on robotic perception and control for autonomous systems. He is currently a Ph.D. fellow at Khalifa University Center for Autonomous Robotics (KUCARS).



**Daniel Gehrig** received his BSc. and MSc. in Mechanical Engineering from the ETH Zurich, Switzerland, in 2019. He is currently with the University of Zurich at the Robotics and Perception Group. His research interests are focused on exploring the intersection of event-based vision, deep learning, and robotics.



**Abdelqader Abusafieh** is currently SVP for Technology & Advanced Materials at Strata Manufacturing PJSC (a Mubadala Company) where he is responsible for driving R&D strategy and technology development programs within Mubadala Aerospace assets including collaboration initiatives with OEMs, technology partners, and academia. Prior to this role, he worked as a Technical Advisor at Mubadala Aerospace & Defense unit for investment activities and Technology and Training initiatives. Dr. Abusafieh received his Master's in Mechanical Engineering from Villanova University his Ph.D. in Materials Engineering from Drexel University. He has several patents and numerous publications and invited seminars. He sits on a number of senior management boards in academia and industry.



**Lakmal Seneviratne** is Professor of Mechanical Engineering and the founding Director of the Centre for Autonomous Robotic Systems (KUCARS) at Khalifa University, UAE. He has also served as Associate Provost for Research and Graduate Studies and Associate VP Research at Khalifa University. Prior to joining Khalifa University, he was Professor of Mechatronics, the founding Director of the Centre for Robotics Research and the Head of the Division of Engineering, at King's College London. He is Professor Emeritus at King's College London. His main research interests are centered on robotics and automation, with particular emphasis on increasing the autonomy of robotic systems interacting with complex dynamic environments. He has published over 400 peer reviewed publications on these topics. He is a member of the Mohammed Bin Rashid Academy of Scientists in the UAE.



**Davide Scaramuzza** (1980, Italy) received a Ph.D. degree in robotics and computer vision from ETH Zurich, Switzerland, in 2008, followed by postdoctoral research at both ETH Zurich and the University of Pennsylvania, Philadelphia, USA. He is a Professor of Robotics and Perception with the University of Zurich, where he does research at the intersection of robotics, computer vision, and machine learning, aiming to enable autonomous, agile navigation of micro drones using standard and neuromorphic event-based cameras. From 2009 to 2012, he led the European project sFly, achieving the first autonomous vision-based navigation of microdrones in GPS-denied environments, which inspired the visual-navigation algorithm of the NASA Mars helicopter. He has served as a consultant for the United Nations on topics such as disaster response and disarmament, as well as the Fukushima Action Plan on Nuclear Safety. He coauthored the book *Introduction to Autonomous Mobile Robots* (MIT Press). For his research contributions, he won prestigious awards, such as a European Research Council (ERC) Consolidator Grant, the IEEE Robotics and Automation Society Early Career Award, an SNF-ERC Starting Grant, a Google Research Award, a Facebook Distinguished Faculty Research Award, and several paper awards. In 2015, he co-founded Zurich-Eye, today Facebook Zurich, which developed the hardware and software tracking modules of the Oculus VR headset, which sold over 10 million units. Many aspects of his research have been prominently featured in wider media, such as *The New York Times*, *The Economist*, *Forbes*, *BBC News*, *Discovery Channel*.



**Yahya Zweiri** (Member, IEEE), obtained his Ph.D. degree from King's College London. He is currently a Professor at the Department of Aerospace Engineering and the Director of the Advanced Research and Innovation Center, Khalifa University, United Arab Emirates. Over the past two decades, he has actively participated in defense and security research projects at institutions such as the Defense Science and Technology Laboratory, King's College London, and the King Abdullah II Design and Development Bureau in Jordan. Dr. Zweiri has a prolific publication record, with over 130 refereed journals and conference papers, as well as ten filed patents in the USA and UK. His primary research focus centers around robotic systems for challenging environments, with a specific emphasis on applied AI and neuromorphic vision systems.